Chemical Science

EDGE ARTICLE

Cite this: *Chem. Sci.*, 2014, **5**, 727

# Directional charge transfer and highly reducing and oxidizing excited states of new dirhodium(II,II) complexes: potential applications in solar energy conversion†

Zhanyong Li,[a] Nicholas A. Leed,[b] Nicole M. Dickson-Karn,[c] Kim R. Dunbar*[a] and Claudia Turro*[b]

Received 23rd August 2013
Accepted 14th October 2013

DOI: 10.1039/c3sc52366g

www.rsc.org/chemicalscience

Two new series of dirhodium(II,II) complexes *cis*-$[Rh_2(\mu\text{-DTolF})_2(L)_2][BF_4]_2$ and *cis*-$[Rh_2(\mu\text{-F-form})_2(L)_2][BF_4]_2$ were synthesized and fully characterized (DTolF = *p*-ditolylformamidinate, F-form = *p*-difluorobenzylformamidinate; L = the chelating diimine ligands dpq (dipyrido[3,2-*f*:2′,3′-*h*]quinoxaline), dppz (dipyrido[3,2-*a*:2′,3′-*c*]phenazine) and dppn (benzo[*i*]dipyrido[3,2-*a*:2′,3′-*h*]quinoxaline). The complexes undergo facile oxidation and exhibit directed ligand-to-ligand charge transfer (LLCT) excited states upon excitation from the corresponding formamidinate to the diimine ligand. Time-resolved studies reveal that the LLCT states decay with lifetimes that range from 16 to 100 ps and generate a longer-lived excited state. For complexes with dpq and dppz ligands, the longer-lived excited state, with lifetimes that range from 40 to 100 ns, has been assigned as $^3$MC (MC = metal-centered) arising from the $Rh_2(\pi^*) \rightarrow Rh_2(\sigma^*)$ transition. In the case of *cis*-$[Rh_2(\mu\text{-DTolF})_2(dppn)_2]^{2+}$ and *cis*-$[Rh_2(\mu\text{-F-form})_2(dppn)_2]^{2+}$, the dppn-centered $^3\pi\pi^*$ excited state is observed from ~10 ps to ~2 ns, but following its decay, the $^3$MC state of each complex is observed with lifetimes of 2.4 and 3.0 μs, respectively. The long lifetimes observed for the dppn complexes is explained by a pre-equilibrium of the low-lying $^3\pi\pi^*$ and $^3$MC states. The excited state oxidation potentials, $E^*_{ox}(^1\text{LLCT})$, for the complexes are calculated to lie between −2.5 and −2.8 V *vs.* SCE and $E^*_{ox}(^3\text{MC}) \sim -1.8$ V *vs.* SCE. The $^1$LLCT excited states of the complexes are also good oxidizing agents, with $E^*_{red}(^1\text{LLCT}) \sim +1.3$ V *vs.* SCE, making them significantly better oxidizing and reducing agents than commonly used Ru(II) complexes.

## Introduction

The excited state redox processes of transition-metal complexes have been explored extensively for solar energy conversion.[1–11] Harnessing the energy of the sun includes the direct generation of electrical current and the production of fuels from abundant sources such as $H_2O$ and acids. The photoactivation of transition-metal complexes to render them reactive with substances that are harmful to the environment are also important and include the reduction of the greenhouse gas $CO_2$,[9] the photo-Fenton reaction to degrade various pollutants,[12] and other photocatalysts for environmental remediation.[13]

The photocatalytic production of $H_2$ from acidic aqueous media has been reported for numerous transition-metal compounds.[2,3,6,10,14,15] In general, the catalytic center is coupled to a photosensitizer to act as the light absorber which then participates in excited state charge transfer reactions to activate the catalyst with regeneration of the sensitizer with a sacrificial donor. The sensitizer and catalyst typically rely on bimolecular electron transfer,[16] but strategies have been developed to covalently tether them in order to improve reactivity.[17–19] Alternatively, the light absorber may first oxidize the sacrificial donor, such that the reduced sensitizer then transfers an electron to the catalyst.[20] An example that is relevant to the present work involves the dirhodium(II,II) complexes, *cis*-$[Rh_2(\mu\text{-}O_2CCH_3)_2(L)_2][O_2CCH_3]_2$ (L = bpy, phen; bpy = 2,2′-bipyridine, phen = 1,10-phenanthroline), which were recently shown to act as catalysts for $H_2$ evolution from $H^+$; the excited state of the photosensitizer, $[Ir(ppy)_2(dtbbpy)]^+$ (ppy = 2-phenylpyridine, dtbbpy = 4,4′-di-*tert*-burtyl-2,2′-bipyridine), oxidizes a sacrificial donor, followed by electron transfer from the reduced sensitizer to the dirhodium catalyst.[21] In this work the identity

[a]*Department of Chemistry, Texas A&M University, USA. E-mail: dunbar@mail.chem.tamu.edu; Fax: +1-979-845-7177; Tel: +1-979-845-7177*

[b]*Department of Chemistry and Biochemistry, The Ohio State University, USA. E-mail: turro.1@osu.edu; Fax: +1-614-292-16858; Tel: +1-614-292-6708*

[c]*Department of Chemistry and Biochemistry, Ohio Northern University, USA*

† Electronic supplementary information (ESI) available: $^1$H NMR spectra, crystal packing diagram and crystallographic refinement parameters and data, electrochemistry, electronic absorption spectra of cations, optimized structures, additional transient absorption data, ground and excited state electronic absorption spectra of $Ir_2(DTolF)_4$ and $Rh_2(DTolF)_4$, calculated orbital contributions and vertical energies of the singlet and triplet excited states. CCDC 937902–937906. For ESI and crystallographic data in CIF or other electronic format see DOI: 10.1039/c3sc52366g

of the active forms of the reduced catalysts are unknown. Other excellent examples of important studies in this vein are the work of Nocera and co-workers, who were able to circumvent the excited state electron transfer steps involving the sensitizer and the catalyst by designing complexes for which both the light absorber and the catalytic unit are installed in the same chromophore.[3,22]

In addition to the conversion of the energy of photons into chemical energy, photoexcited molecules (dyes) are able to inject electrons into the conduction band (CB) of wide band gap semiconductors resulting in the generation of current.[1,4,5,7,23,24] This strategy has been used extensively in dye-sensitized solar cells (DSSC) where typical dyes are Ru(II) complexes and the anode is $TiO_2$. Similarly, photoexcited dyes that are good excited state oxidizing agents may inject holes into the valence band (VB) of p-type semiconductors, such as NiO.[25–28] Recently there has been increased interest in the development of tandem cells wherein both the anode and cathode are involved in charge transfer with a sensitizer within the same DSSC,[29,30] as well as in solar cells coupled to chemical transformations.[4] The use of new electrodes to improve the efficiency of DSSCs is desirable,[31,32] but the use of materials with higher energy conduction bands is limited owing to the relatively low excited state oxidation potentials of the dyes currently in use.[33,34]

The present work focuses on the synthesis and characterization of *cis*-$[Rh_2(\mu\text{-DTolF})_2(L)_2][BF_4]_2$ and *cis*-$[Rh_2(\mu\text{-F-form})_2(L)_2][BF_4]_2$ (DTolF = *p*-ditolylformamidinate, F-form = *p*-difluorobenzylformamidinate; L = chelating diimine ligand, dpq = dipyrido[3,2-*f*:2′,3′-*h*]quinoxaline, dppz = dipyrido[3,2-*a*:2′,3′-*c*]phenazine, dppn = benzo[*i*]dipyrido[3,2-*a*:2′,3′-*h*]quinoxaline) and the investigation of their excited state properties. These complexes, the structures of which are depicted in Fig. 1, were chosen based on our prior finding that $Rh_2(form)_4$ (form = formamidinate ligands with various substituents) exhibit highly reducing excited states capable of transferring electrons to alkyl halides *via* an outer-sphere mechanism.[35] The photophysical and redox properties of the new complexes were investigated, and the data reveal highly reducing and oxidizing ligand-to-ligand charge transfer (LLCT) excited states; the hole and electron are positioned across the dimetal core and are localized on the formamidinate and diimine ligands, respectively. This charge disposition may aid in accomplishing both electron injection into $TiO_2$ or another electrode material with a higher energy CB, while the same complex may undergo hole injection into the VB of NiO or another p-type semiconductor after light absorption. In this manner, complexes with appropriate substituents for electrode binding, such as –COOH,[1,4,5,7] may be used to sensitize charge injection into both electrodes.

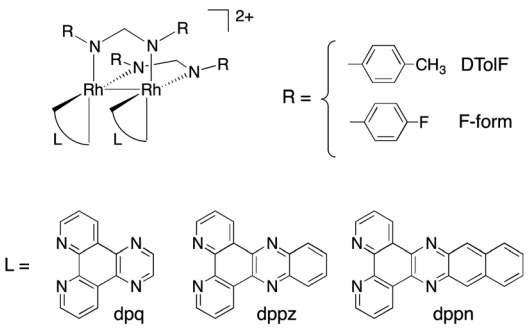


| Complex | R | L |
|---|---|---|
| **1** | DTolF | dpq |
| **2** | DTolF | dppz |
| **3** | DTolF | dppn |
| **5** | F-form | dpq |
| **6** | F-form | dppz |
| **7** | F-form | dppn |

Fig. 1 Schematic representation of the molecular structures of selected complexes.

## Results and discussion

### X-Ray crystallography

***cis*-$[Rh_2(DTolF)_2(dppz)_2(CH_3CN)][BF_4]_2$ (2).** The molecular structure of **2** consists of a cationic dirhodium unit bridged by two $[DTolF]^-$ ligands in a cisoid disposition (Fig. 2a). Two outer-sphere $[BF_4]^-$ anions are present as well. Each Rh(II) center is further chelated by a dppz ligand that occupies two equatorial positions (Fig. 2a). One of the two axial positions is occupied by a solvent acetonitrile molecule with a bond distance of Rh–$N(CH_3CN_{ax})$ of 2.158(6) Å. The occupation of only one axial site is not uncommon for dirhodium(II,II) compounds with $[DTolF]^-$ ligands and is attributed to its strong electron donating ability and the steric hindrance afforded by the bulky tolyl groups.[36] The Rh–Rh bond distance is 2.597(1) Å which is comparable to that found in the related compounds *cis*-$[Rh_2(DTolF)_2(CH_3CN)_6][BF_4]_2$,[36a] *cis*-$[Rh_2(DTolF)_2(bpy)(CH_3CN)_3][BF_4]_2$, and *cis*-$[Rh_2(DTolF)_2(bpy)_2(CH_3CN)][BF_4]_2$.[36b] The Rh–N bond distances

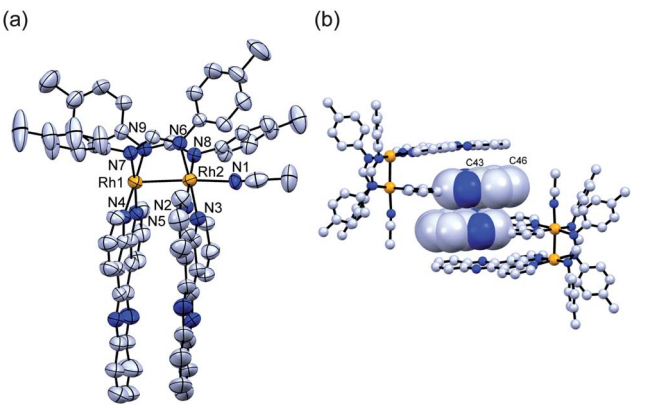


Fig. 2 Crystal structure of **2** showing (a) thermal ellipsoid plot of the cation drawn at 50% probability level; important bond distances in (Å) and dihedral angles in (°): Rh1–Rh2 2.597(1), Rh1–N4 2.041(5), Rh1–N9 2.015(5), Rh2–N1 2.158(6), Rh2–N6 2.045(6), N4–Rh1–Rh2–N2 −15.6(2), N7–Rh1–Rh2–N6 −15.7(2); and (b) the crystal packing of the cations showing intermolecular π-stacking; the $[BF_4]^-$ anions and hydrogen atoms are omitted for the sake of clarity. Colors for thermal ellipsoids: C: gray, N: blue, Rh: orange.

to the dppz ligands range from 2.040(5) to 2.060(2) Å, which are slightly longer than those reported for *cis*-$[Rh_2(\mu\text{-}O_2CCH_3)_2(dppz)_2][O_2CCH_3]_2$.[37] The longer Rh–diimine N bond in **2** is explained on the basis of a stronger *trans* influence induced by the more electron-rich $[DTolF]^-$ ligand as compared to $[CH_3CO_2]^-$.

The presence of the Rh–Rh bond brings the two dppz ligands into close proximity, which leads to splaying from a parallel alignment to decrease steric repulsion. The twist angle of the two dppz ligands away from the eclipsed geometry is 15.6°, similar to the angle of 13° found in *cis*-$[Rh_2(\mu\text{-}O_2CCH_3)_2(dppz)_2][O_2CCH_3]_2$.[37] The view along the *b* axis of the crystal packing diagram of **2** (Fig. 2b), reveals π-stacking interactions of the dppz ligands between two adjacent dirhodium cations along the *c* axis. Since these ligands are not parallel to each other, no definitive distances can be measured between the two planes defined by them, but we note that the distances between C43 and C46 and the plane defined by C43–C44–C45–C46–C47–C48 in the adjacent dppz ligands are 3.47 and 3.42 Å, respectively, as depicted in Fig. 2b. Such short intermolecular distances are indicative of π-stacking interactions between the two adjacent molecules. The crystal packing diagrams of **2** viewed along the *b* and *c* axes are provided in Fig. S4 (ESI†).

***cis*-$[Rh_2(DTolF)_2(dppn)_2Cl][BF_4]\cdot Et_2O\cdot 3CH_3CN$ ($3\cdot Et_2O\cdot 3CH_3CN$).** The cation in complex **3** crystallizes in the space group $P\bar{1}$ along with a tetrafluoroborate anion as well as three acetonitrile and one diethyl ether interstitial solvent molecules. The coordination sphere of the Rh(II) centers is similar to that found in **2** except that one axial position is occupied by a $Cl^-$ ligand (Fig. 3). The Rh–Cl distance of 2.4562(7) Å is comparable to that reported for $[Rh_2(1,3\text{-diisocyanopropane})_4Cl_2]Cl_2$, in which Rh–Cl (ax) is 2.4472(8) Å,[38] but is significantly longer than the Rh–N ($CH_3CN_{ax}$) bond length in **2**, which is not surprising given the larger size of the $Cl^-$ ion. The Rh–Rh bond distance is 2.5818(3) Å and the Rh–N (dppn) bond distances are in the range of 2.032(2)–2.053(3) Å, comparable the corresponding metrical parameters found in **2**. The two dppn ligands are twisted away from the eclipsed configuration with a dihedral angle of ~28°. This value is significantly larger than was found for the dppz ligands in **2**, indicating stronger repulsion between the two adjacent dppn ligands in **3**.

***cis*-$[Rh_2(F\text{-}form)_2(dpq)_2(CH_3CN)_2][BF_4]_2$ (5).** The molecular structure of the cationic unit in **5** depicted in Fig. 4 is similar to that of **2**, but with both axial positions being occupied by $CH_3CN$ ligands as a result of the smaller size and less electron-rich nature of the $[F\text{-form}]^-$ *vs.* the $[DTolF]^-$ ligands. The Rh–Rh distance is 2.5991(9) Å in **5**, the Rh–N distances in the $[F\text{-form}]^-$ ligand range from 2.034(5) to 2.052(5) Å, and the Rh–N (dpq) distances are in the range of 2.035(3)–2.053(3) Å, similar to the Rh–N (dppz) lengths in **2**. The internal twist angles away from the eclipsed geometry of the two dpq ligands defined by N5–Rh1–Rh2–N7 and N6–Rh1–Rh2–N8 are −18.6(1) and −18.9(1)°.

***cis*-$[Rh_2(F\text{-}form)_2(dppz)_2(CH_3CN)_2][BF_4]_2$ (6).** Compound **6** crystallizes in the same space group as **5**, namely $P\bar{1}$. The thermal ellipsoid plot of the cationic unit is shown in Fig. 5a. Both axial positions of **6** are occupied by solvent $CH_3CN$ molecules with Rh–N distances of 2.210(6) and 2.256(6) Å. The Rh–Rh bond distance, 2.6190(9) Å, is slightly longer than the corresponding distance in **5**. The Rh–N ($[F\text{-form}]^-$) bond distances are in the range 2.043(5)–2.065(5) Å, similar to those found in **5**. The Rh–N (dppz) bond distances are ~2.06 Å, similar to those in **2**. The two dppz ligands in one molecule of **6** are twisted away from the eclipsed configuration with dihedral angles defined by N8–Rh2–Rh1–N6 and N7–Rh2–Rh1–N5 of 17.4(2) and 16.8(2)°.

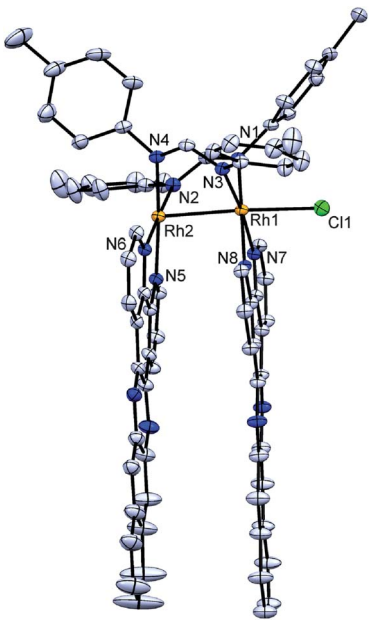


Fig. 3 Thermal ellipsoid plot of **3** drawn at 50% probability level. Hydrogen atoms, $[BF_4]^-$ anion, and interstitial solvent molecules are omitted for the sake of clarity. Important bond distances (Å) and dihedral angles (°): Rh1–Rh2 2.5818(3), Rh1–Cl1 2.4562(7), Rh1–N7 2.048(3), Rh2–N4 2.041(3); N8–Rh1–Rh2–N6 28.29(9), N1–Rh1–Rh2–N2 25.8(1). Colors for thermal ellipsoids: C: gray, N: blue, Cl: green, Rh: orange.

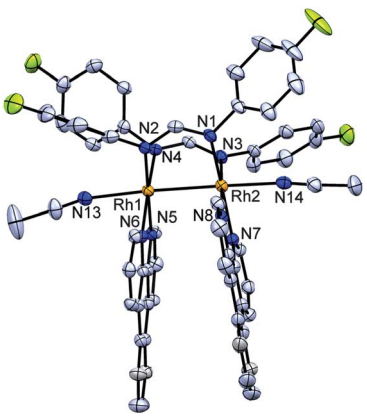


Fig. 4 Thermal ellipsoid plot of **5** at the 50% probability level; the anions, hydrogen atoms are omitted for the sake of clarity. Important bond distances (Å) and dihedral angles (°): Rh1–Rh2 2.5991(9), Rh1–N13 2.233(3), Rh1–N4 2.042(3), Rh2–N8 2.045(3), N6–Rh1–Rh2–N8 −18.9(1), N2–Rh1–Rh2–N1 −14.4(1). Colors for thermal ellipsoids: C: gray, N: blue, F: yellow, Rh: orange.

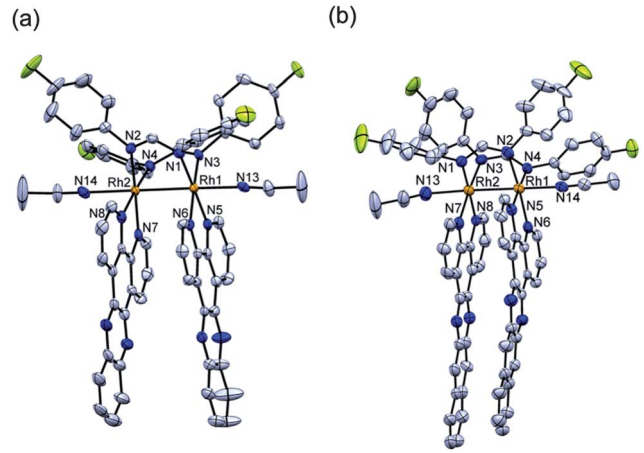


Fig. 5 Thermal ellipsoid plots at 50% probability level. The anions, hydrogen atoms and interstitial solvent molecules are omitted for the sake of clarity (a) **6**, representative bond distances (Å) and dihedral angles (°): Rh1–Rh2 2.6190(9), Rh1–N13 2.210(6), Rh1–N3 2.043(5), Rh1–N1 2.059(4), N1–Rh1–Rh2–N2 14.0(2), N5–Rh1–Rh2–N7 17.4(2); and (b) **7**, representative bond distances (Å) and dihedral angles (°): Rh1–Rh2 2.615(1), Rh1–N2 2.056(5), Rh1–N14 2.202(7), Rh2–N7 2.055(4), N2–Rh1–Rh2–N1 −17.4(2), N5–Rh1–Rh2–N7 −21.7(2). Colors for thermal ellipsoids: C: grey, N: dark blue, F: yellow, Rh: orange.

***cis*-$[Rh_2(F\text{-form})_2(dppn)_2(CH_3CN)_2][BF_4]_2\cdot 2CH_3CN$ ($7\cdot 2CH_3CN$).** As in the case of the dirhodium cations in **5** and **6**, both axial positions are occupied by $CH_3CN$ ligands in **7** with bond distances of 2.202(7) and 2.245(9) Å (Fig. 5b). The Rh–Rh bond distance is 2.615(1) Å, slightly longer than those found in **5** but comparable to that in **6**. The Rh–N ($[F\text{-form}]^-$) bond distances are in the range 2.047(5)–2.069(4) Å similar to that for **5** and **6**. The Rh–N (dppn) bond distances range from 2.042(8) to 2.064(6) Å, comparable to those in **5**. Much larger distortions between the two diimine ligands is evident in **7** as compared to that of **5** and **6**, with the angles defined by N5–Rh1–Rh2–N7 and N6–Rh1–Rh2–N8 being −21.7(2) and −21.8(2)°, respectively, due to considerable repulsion between the two dppn ligands.

## Electronic absorption and electrochemistry

The absorption maxima and intensities of **1–3** and **5–7** in $CH_3CN$ are listed in Table 1. The relatively strong transitions observed for all complexes between 290 and 420 nm are similar to those for the free diimine ligand. The dpq ligand absorbs at 254 nm ($\varepsilon = 53\,000\ M^{-1}\ cm^{-1}$) in $CHCl_3$, which compares well to the maxima of **1** and **5** at 289 nm ($\varepsilon = 54\,000\ M^{-1}\ cm^{-1}$) and 291 nm ($\varepsilon = 50\,000\ M^{-1}\ cm^{-1}$), respectively. Similarly, dppz and dppn exhibit maxima at 370 nm ($\varepsilon = 17\,200\ M^{-1}\ cm^{-1}$) and 414 nm ($\varepsilon = 12\,500\ M^{-1}\ cm^{-1}$), respectively, in $CHCl_3$,[39] similar to those measured for **2** and **6** (~370 nm) and **3** and **7** (~418 nm), respectively (Table 1). Owing to these similarities, the lowest energy peaks are assigned as ligand-centered diimine $^1\pi\pi^*$ transitions. It is noted that these $^1\pi\pi^*$ transitions are also present in the related complexes *cis*-$[Rh_2(\mu\text{-}O_2CCH_3)_2(L)(\eta^1\text{-}O_2CCH_3)(CH_3OH)]^+$ (L = dpq, dppz, dppn), *cis*-$[Rh_2(\mu\text{-}O_2CCH_3)_2(dppz)_2]^{2+}$, *cis*-$[Rh_2(\mu\text{-}O_2CCH_3)_2(dppn)_2]^{2+}$,[37,40] as well as in Ru(II) and Os(II) complexes containing dpq, dppz and dppn ligands.[39,41–46] Intense peaks are observed at higher energies in the 250–280 nm rage, namely at 256 nm for **1** and **5**, 275 nm for **2** and **6**, and 261 nm for **3** and **7**. Although a small dependence is apparent as a function of the diimine ligand, it is likely that these are metal-centered transitions involving orbitals participating in bonding interactions with the diimine ligands. Similar transitions are observed in $Rh_2(F\text{-form})_4$ at 230 nm ($\varepsilon = 42\,000\ M^{-1}\ cm^{-1}$) and 275 nm ($\varepsilon = 23\,900\ M^{-1}\ cm^{-1}$) and in $Rh_2(DTolF)_4$ at 265 nm ($\varepsilon = 61\,800\ M^{-1}\ cm^{-1}$) in $CH_3CN$.

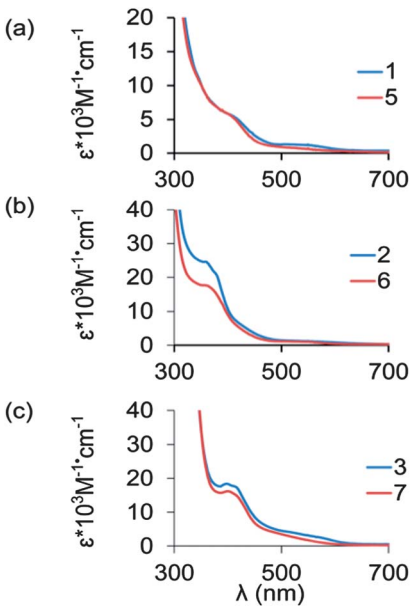


Fig. 6 Electronic absorption spectra of **1** and **5** (a), **2** and **6** (b), and **3** and **7** (c) in $CH_3CN$.

Table 1 Electronic absorption maxima, $\lambda_{abs}$, molar absorptivities, $\varepsilon$, and reduction potentials for **1–3** and **5–7** in $CH_3CN$

| Complex | $\lambda_{abs}$/nm ($\varepsilon/10^3\ M^{-1}\ cm^{-1}$) | $E_{1/2}$/V[a] |
|---|---|---|
| **1** | 256 (98), 289 (54), 525 (1.3) | −1.55, −1.36, −1.03,[b] −0.40, +1.05, +1.59[c] |
| **2** | 276 (143), 368 (25), 541 (1.3) | −1.49, −1.16, −0.94,[b] −0.42, +1.06,[b] +1.64[c] |
| **3** | 261 (100), 314 (110), 418 (17), ~553 (3.0) | −1.50, −0.92, −0.67,[b] −0.40, +1.06,[b] +1.55[c] |
| **5** | 256 (116), 291 (50), 520 (0.80) | −1.55, −1.29, −0.98,[b] −0.45, +1.17,[b] +1.68[c] |
| **6** | 275 (107), 371 (17), 537 (1.0) | −1.40, −1.13, −0.91,[b] −0.39, +1.18,[b] +1.74[c] |
| **7** | 260 (92), 315 (101), 419 (14), ~525 (1.8) | −1.39, −0.88, −0.61,[b] −0.38, +1.16,[b] +1.73[c] |

[a] *vs.* Ag/AgCl; 0.1 M[*n*-$Bu_4N$][$PF_6$]; 0.2 V $s^{-1}$. [b] Quasi-reversible. [c] Irreversible.

In addition to the higher energy transitions there is a tail in the absorption profile for each complex that extends to lower energies; the data are compiled in Table 1 and illustrated in Fig. 6. The dependence of the absorption maxima on the identity of the diimine ligands for each series taken together with the intensities being in the ~1 to 3 × $10^3$ $M^{-1}$ $cm^{-1}$, point to the assignment of these lower energy peaks as being charge-transfer transitions from the metal or formamidinate to the diimine ligands. Such charge transfer features are also observed in the related $[Rh_2(\mu\text{-}O_2CCH_3)_2(L)_2]^{2+}$ complexes where L is dpq, dppz and dppn with maxima in the range 609–620 nm with similar intensities ($\varepsilon$ = 1100–3800 $M^{-1}$ $cm^{-1}$).[40] The increased electron donation from the formamidinate ligands to the bimetallic core as compared to acetate is consistent with the lower energies of these charge-transfer transitions in **1–3** and **5–7**. Furthermore, this transition is observed at lower energies for the DTolF complexes as compared to the corresponding F-form compounds, which supports the fact that the formamidinate ligands participate in the transition.

The observed redox couples measured for **1–3** and **5–7** are listed in Table 1. A redox couple is apparent at approximately −0.4 V *vs.* Ag/AgCl in **1–3** and **5–7** (Table 1, Fig. S5 for complex **6**, ESI†). This process represents an oxidation of the complexes which has been confirmed by a color change observed in the presence of oxidizing agents such as TCNQ, 7,7,8,8-tetracyanoquinonedimethane, ($E'$ = −0.14 *vs.* SCE in $CH_3CN$, $\Delta G$ = −0.30 V), $AgBF_4$ in $CH_3CN$ ($E'$ = +0.44 V *vs.* SCE, $\Delta G$ = −0.88 V) and $NOBF_4$ ($E'$ = +1.03 V *vs.* SCE, $\Delta G$ = −1.47 V).[47] Following the oxidation of **1** and **2** with TCNQ, the IR stretch at ~2186 $cm^{-1}$ is observed which is known to correspond to the TCNQ radical anion, $TCNQ^-$.[48] The products of the reactions of **1** and **2** with $NOBF_4$ were isolated and their absorption spectra are shown in Fig. S6 (ESI†). The facile oxidation of these dirhodium(II,II) complexes is not unexpected given the presence of the electron-rich formamidinate ligands.

The second oxidation process is observed at +1.06 V *vs.* Ag/AgCl for the DTolF complexes **1–3** and at +1.17 V *vs.* Ag/AgCl for the F-form series **5–7** (Table 1). This couple is reversible in the case of **1** and quasi-reversible for **2**, **3** and **5–7** and is independent of the nature of the diimine ligand in each series but dependent on the substituents of the formamidinate ligand. As expected, the complexes equipped with DTolF ligands are more easily oxidized than those containing the electron-withdrawing fluoride substituents, F-form (Table 1). The difference of ~0.1 V for the DTolF and F-form complexes is in agreement with the difference in the second oxidation potentials of $Rh_2(DTolF)_4$ and $Rh_2(F\text{-form})_4$ compounds of 0.14 V; the $E_{1/2}$ values are +0.85 and +0.99 V *vs.* SCE, respectively.[49] The third oxidation process is irreversible for all of the complexes with $E_{pa}$ ~ +1.6 V *vs.* Ag/AgCl for **1–3** and ~ +1.7 V *vs.* Ag/AgCl for **5–7** (Table 1). The 0.1 V difference between the two series is also consistent with removal of the electron from an orbital with significant formamidinate character.

The first reduction event occurs at −1.03, −0.94 and −0.67 V *vs.* Ag/AgCl for **1**, **2** and **3** (Table 1), respectively, and is clearly dependent on the nature of the diimine ligand. These values are similar to those found for the corresponding F-form complexes **5**, **6** and **7**, at −0.98, −0.91 and −0.61 *vs.* Ag/AgCl (Table 1). The trends for each series of complexes, considering the fact that the diimine ligand L is easier to reduce in the order dppn > dppz > dpq, is consistent with the first reduction being centered on this ligand. These values are also comparable to those reported for Ru(II) complexes with dpq, dppz and dppn ligands.[39,44,50] The potential of the second reduction process is also dependent on the diimine ligand L (Table 1), which is also the case for Ru(II) complexes, it may be assigned to the placement of an electron on the remaining neutral diimine ligand.[44,50] A third reduction process is observed in the range of −1.39 to −1.55 V *vs.* Ag/AgCl for **1–3** and **5–7**, in accord with a metal-centered reduction. On the basis of the typical electronic structure of $d^7$–$d^7$ paddlewheel complexes, it is reasonable to expect that the third reduction corresponds to the population of the $Rh_2(\sigma^*)$ orbital.[49] These values are similar to the corresponding data for $Rh_2(DTolF)_4$ at −1.23 V *vs.* Ag/AgCl that do not possess diimine ligands.[49]

## Electronic structure calculations

Computational studies of the DTolF and F-form series of compounds were performed in order to gain a deeper understanding of their electronic structures. Geometric parameters for the gas-phase optimizations were obtained from the crystal structures of **2** and **5–7**. For the calculations of **1–3**, $CH_3CN$ ligands were placed in both axial positions because only one set of dpq, dppz and dppn resonances was observed in the solution $^1H$ NMR spectra, indicating a symmetrical coordination environment. The calculated structures of **5–7** are depicted in Fig. S7 (ESI†). Comparisons of the important bond distances between X-ray data and the computational modeling for these complexes are summarized in Table S2 (ESI†).

The calculated MO diagrams of **1–3** and **5–7** are shown in Fig. 7, and the contributions to the orbitals from the metal and the ligands are listed in Tables S3 and S4 (ESI†). The HOMO and HOMO−1 are of all the complexes are calculated to contain significant contributions from the formamidinate ligands. In

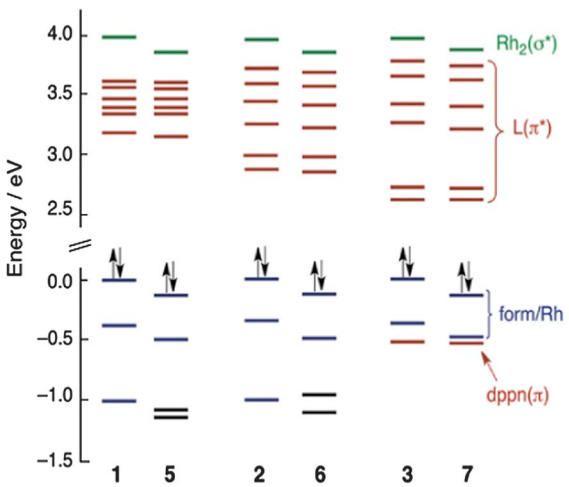


Fig. 7 Calculated MO diagrams for **1–3** and **5–7**; the HOMO of **1** was arbitrarily set to 0.0 eV.

general, the HOMO of each complex exhibits ~63% contribution from the DTolF or F-form ligand and ~33% from Rh, whereas the HOMO−1 typically contains ~84% formamidinate and ~10% Rh character (Tables S3 and S4, ESI†). Consistent with the ligand contributions to these orbitals, the relative energy of the HOMO and HOMO−1 vary with the nature of the formamidinate ligand by ~0.1 eV. It should be noted that in the dppn complexes **3** and **7** the HOMO−2 is localized on the dppn ligand.

As depicted in Fig. 7, the electron densities of the LUMO to LUMO+5 in **1–3** and **5–7** are centered on the corresponding diimine ligand. The relative energies of the LUMOs are consistent with the ease of reduction of the complexes, *i.e.*, **1** and **5** are more difficult to reduce than **2** and **6**, and **3** and **7** are easier to reduce (Table 1). In each complex, the LUMO+6 is calculated to possess 66% $Rh_2(\sigma^*)$ character with 15% contribution from $CH_3CN_{ax}$ ligands. The electron density contributions to the HOMO and LUMO levels of **1** are depicted in Fig. 8 and are representative of those calculated for **2**, **3**, and **5–7**.

The vertical energies and orbital contributions for the lowest eight singlet excited states of **1–3** and **5–7** are listed in Tables S5 and S6 (ESI†), respectively. In all complexes, the major contribution to the lowest energy singlet excited state (≥82% in **1–3** and ≥78% in **5–7**) corresponds to the transfer of electron density from the HOMO to the LUMO of each complex. Because the HOMO exhibits a high degree of formamidinate character (~66%) and the LUMO is localized on the corresponding diimine ligands, this state may be assigned as a ligand-to-ligand charge transfer ($^1$LLCT), however, the oscillator strength associated with this transition must arise from a MLCT transition stemming from the partial metal character of the HOMO. The calculated oscillator strengths, *f*, of the vertical transitions from the ground state, $^1$GS, to the lowest energy state, $^1$LLCT state are listed in Tables S5 and S6 (ESI†), and the calculated transition energies are in good agreement with the experimental maxima in these complexes (Table 1). For example, the calculated energy of the $^1$GS → $^1$LLCT transitions in **1** and **5** are at 536 and 518 nm, which compare well with the experimental maxima of 525 and 520 nm, respectively (Table 1 and Fig. 6a). The calculated maxima for the lowest energy $^1$GS → $^1$LLCT transitions at 562 and 537 nm for **2** and **6**, respectively, are red shifted from those of **1** and **5** (Tables S5 and S6, ESI†), consistent with ease of reduction for the diimine ligands in the former as compared to the latter compounds (Table 1). The low energy transitions of **1**, **2** and **3** are red-shifted relative to those of the corresponding F-form complexes, **5**, **6** and **7**, respectively, a trend that is rationalized by the fact that DTolF is a better electron donor than is F-form which influences the transitions which involve removal of electron density from orbitals with significant formamidinate character, such as the HOMO.

## Transient absorption spectroscopy

The identity and kinetics of the excited states of **1–3** and **5–7** were investigated using transient absorption (TA) spectroscopy. The TA spectra of **1** collected at various delay times following excitation with a 310 nm, 300 fs pulse in $CH_3CN$ are shown in Fig. 9a and b. It should be noted that the spectral profiles and kinetics are similar to those collected with 375 and 385 nm (Fig. S10, ESI†). A strong feature that absorbs in the 360–520 nm range is evident at early times in the TA spectrum of **1** from 0.3 to 20 ps (Fig. 9a and S8, ESI†). The apparent peak at ~460 nm in the spectrum of **1** is created by the superposition of the ground-state bleach, such that the positive spectrum arising from the transient species is expected to be relatively featureless, with intensity increasing from 600 to 360 nm. A similar absorption profile is also observed for $Rh_2(DTolF)_4$ at early times, believed to arise from DTolF → $Rh_2$ LMCT. Because of the ease of oxidation of the complexes, the TA spectrum of **1** was collected in the region further into the red (640–730 nm) in order to establish that the spectral features are not due to photooxidation of the complex (Fig. 9b). Photooxidation is accompanied by the generation of a solvated electron in polar solvents which is expected to recombine with $[\mathbf{1}]^+$ within the solvent cage. The spectrum in Fig. 9b does not exhibit the strong absorption with increasing intensity from 600 to 800 nm, that is well established

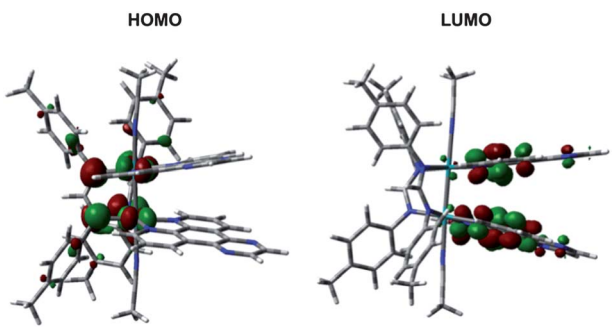


Fig. 8 Electron density maps of the HOMO and LUMO of **1** drawn with isovalue = 0.04.

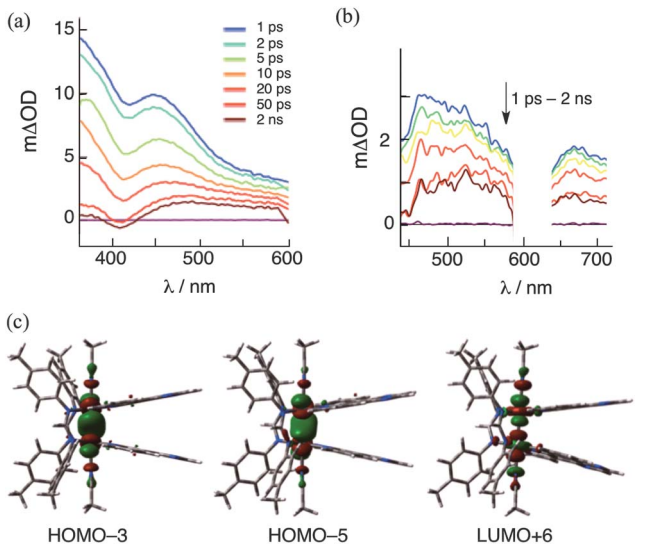


Fig. 9 Transient absorption spectra of **1** in $CH_3CN$ collected at 1 ps to 2 ns following a 310 nm, 300 fs excitation pulse between (a) 360 and 600 nm and (b) 440 and 720 nm, (c) electron density of the HOMO−3, HOMO−5 and LUMO+6 (isovalue = 0.04).

for the solvated electron,[51] such that photoionization can be ruled out. The spectrum in Fig. 9b, however, is consistent with the observed broad absorption from 600 to 750 nm observed for the cation of **1**, $[\mathbf{1}]^+$, shown in Fig. S6 (ESI†) which is expected to correspond to removal of an electron from a HOMO with significant DTolF character. Therefore, the spectral profile of the excited state of **1** observed between 0.3 and 20 ps exhibits features of reduced dpq ($\lambda \leq 400$ nm) and oxidized DTolF (~460 nm), consistent with a DTolF → dpq LLCT excited state.

The decays following the excitation of **1** at both 370 and 460 nm can be fitted to biexponential functions with $\tau_1 = 4$ ps and $\tau_2 = 20$ ps; no spectral changes were observed between 0.3 and 1.0 ps (Fig. S8, ESI†). Since the spectral features before 4 ps are similar to those between 5 and 20 ps, the 4 ps component can be attributed to vibrational cooling. Following the decay of the LLCT state of **1**, a broad but weaker absorption is apparent, with little change between 50 ps and 2 ns (Fig. 9a and b). The TA spectrum of this species collected using 355 nm (fwhm ~ 8 ns) excitation decays monoexponentially with $\tau \sim 40$ ns. The signal of this transient is rather featureless, with an apparent maximum in the 480–520 nm range. Since the strong absorption of the dpq radical anion in the 360–400 nm range is absent (Fig. 9a), this long-lived species must be due to a different electronic state that does not involve charge transfer to the dpq ligand. It should also be noted that excitation of **1** with 385 nm (fwhm = 300 fs) results in similar spectral features and kinetics, indicating that the high energy of the pump pulse in Fig. 9a and b does not play a role in transient species observed and their decays.

The long-lived state of **1**, with $\tau \sim 40$ ns is assigned to the lowest energy triplet excited state of the complex. DFT calculations reveal that the lowest energy state in the triplet manifold has contributions from the HOMO−3 to the LUMO+6 (57.0%) and from the HOMO−5 to the LUMO+6 (35.6%), with a vertical energy of 12 240 $cm^{-1}$ from the minimized singlet ground state (Table S7, ESI†). Inspection of the electron density plots of the HOMO−3 and HOMO−5 MOs reveals that they are $Rh_2(\pi^*)$ in nature with 78 and 77% Rh character, respectively (Fig. 9c). The LUMO+6 is mostly $Rh_2(\sigma^*)$, with contribution from Rh (66%), $CH_3CN_{ax}$ ligands (15%), and DTolF (11%), also shown in Fig. 9c. Therefore, the lowest energy triplet state is calculated as metal-centered ($^3$MC) $Rh_2(\pi^*) \rightarrow Rh_2(\sigma^*)$. The dynamics and assignments for the related complex **5** parallel those of **1**, with vibrational cooling that decays with $\tau = 7$ ps, and lifetimes of the LLCT and $^3$MC states of 100 ps and 100 ns, respectively (Fig. S8 and S9, ESI†), with the $^3$MC state as the lowest energy triplet 11 990 $cm^{-1}$ above the ground state.

It is tempting to assign the short-lived states of **1** and **5**, with lifetimes of 20 and 100 ps, respectively, to singlet LLCT states which then undergo intersystem crossing to generate the $^3$MC excited state of each complex. This scenario is typical for organic molecules, but it is imperative to bear in mind that the intersystem crossing (ISC) rates in transition-metal complexes are typically in the sub-picosecond range.[52] For example, ISC takes place in ~15–40 fs in $[Ru(bpy)_3]^{2+}$,[53,54] is complete in <1 ps in other Ru(II) complexes investigated by us and others,[55–57] and ranges from 15 to 85 fs in $[ReX(CO)_3(bpy)]^+$ (X = Cl, Br, I) complexes.[58] Sub-picosecond ISC rates were also reported for first-row transition-metal complexes, including $Cr(acac)_3$ (acac = acetylacetonate),[59] $[Fe(bpy)_3]^{2+}$,[60] and $[Fe(phen)_3]^{2+}$.[61] Therefore, it is also possible that ISC is faster than internal conversion and vibration cooling in **1**, the result of which is the simultaneous population of the $^3$LLCT and $^3$MC states. Notable exceptions, however, appear in the literature for bimetallic complexes, including quadruply-bonded $d^4$–$d^4$ $Mo_2$(II,II) and $W_2$(II,II) complexes,[62] $d^8$–$d^8$ $[Pt_2(P_2O_5H_2)_4]^{4-}$,[63,64] and $d^8$–$d^8$ $Rh_2$(I,I) isocyanide systems.[65] In addition, an increase in the ISC rate by an order of magnitude was reported for $Cr(t\text{-Bu-acac})_3$ (*t*-Bu-acac = monoanionic form of 2,2,6,6-tetramethyl-3,5-heptanedione) as compared to $Cr(acac)_3$, ascribed to the role of a low-frequency excited state vibration in the latter that is not present in the former in the evolution of Franck–Condon excited state after excitation.[59b] Additional experiments are currently underway to investigate the multiplicity of the short-lived LLCT state in **1** and **5**, as well as in **2**, **3**, **6** and **7** discussed below.

A similar interpretation can be applied to the positive transient absorption features of **2** and **6** in Fig. 10a and S9b (ESI†) respectively (early times shown in Fig. S8, ESI†). The transient spectra of both complexes exhibit strong absorptions with two maxima in the 380–530 nm range at early times (<50 ps); the peak at ~400 nm is likely to be associated with the reduced dppz ligand,[66] whereas the broader absorption at ~460 nm can be ascribed to the oxidized formamidinate ligand also observed in the spectra of $Rh_2(DTolF)_4$ and $Rh_2(F\text{-form})_4$. Given these observations we assign the transient to the LLCT excited state for each complex (Fig. 10a, S9b, and S8, ESI†). The time-resolved spectra recorded for **2** in Fig. 10a decay biexponentially with $\tau_1 = 4$ ps and $\tau_2 = 17$ ps fitted at 405 and 460 nm to generate a longer-lived triplet state with 2 ns < $\tau$ < 10 ns (Fig. 10a). The spectral features of this long-lived transient (see trace collected at 2 ns in Fig. 10a) are similar to those of **1** assigned as the corresponding $^3$MC state (Fig. 10a). Moreover, the calculated lowest energy triplet state corresponds to $Rh_2(\pi^*) \rightarrow Rh_2(\sigma^*)$ (Table S7, ESI†). The assignment of the 17 ps component as the LLCT state is consistent with the spectral features of the cation of **2**, $[\mathbf{2}]^+$, isolated from the reaction of **2** with $NOBF_4$ (Fig. S6, ESI†), as well as the absorption of reduced dppz and related ligands. The spectral features of the related dppz-containing complex **6** are similar to those of **2** (Fig. S9b, ESI†), but with vibrational cooling that decays with a time constant of 8 ps, LLCT state with $\tau = 40$

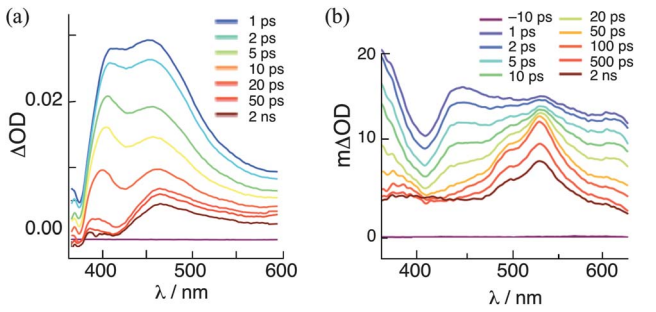


Fig. 10 Transient absorption spectra of (a) **2** and (b) **7** in $CH_3CN$ ($\lambda_{exc}$ = 310 nm, fwhm = 300 fs).

ps (at 445 nm) and $^3$MC state with $\tau \sim 80$ ns; the latter data were acquired on the nanosecond transient absorption system ($\lambda_{exc} =$ 355 nm, fwhm $\sim$ 8 ns) and calculations reveal that, as in the cases of **1**, **2** and **5**, the lowest energy triplet state can be ascribed to $Rh_2(\pi^*) \rightarrow Rh_2(\sigma^*)$ (Table S7, ESI†).

The transient absorption spectrum of **7** shown in Fig. 10b is markedly different than those of **1**, **2**, **5** and **6** and features a strong absorption with a maximum at 540 nm that becomes prominent at $t > 10$ ps. This feature is known to correspond to the long-lived $^3\pi\pi^*$ excited state of the dppn ligand, but, at shorter times (<10 ps), the spectrum is similar to those of **5** and **6** and the intensity at 450 nm can be fitted to a biexponential decay with $\tau_1 = 5$ ps and $\tau_2 = 36$ ps. These two components are assigned to vibrational cooling and to the decay of the F-form $\rightarrow$ dppn LLCT excited state, respectively. The $^3\pi\pi^*$ excited state of the dppn ligand with a maximum at 540 nm exhibits $\tau = 33$ μs in $[Ru(bpy)_2(dppn)]^{2+}$,[67] $\tau = 2.4$ to 4.1 μs in *cis*-$[Rh_2(\mu\text{-}O_2CCH_3)_2(dppn)(L)]^{2+}$ (L = diimine ligand),[68] and $\tau = 20$–24 μs in the related complexes possessing the pydppn ligand (pydppn = 3-(pyrid-2′-yl)-4,5,9,16-tetraazadibnzo[*a*,*c*]naphthacene).[69] In the case of **7**, however, the signal at 540 nm exhibits a decay lifetime of 460 ps fitted from 20 ps to 2 ns, with a shorter component of 4 ps at earlier delay times.

Nanosecond transient absorption experiments reveal a long-lived excited state in **7** with $\tau = 2.4$ μs (Fig. 11a), but this species does not exhibit the strong positive feature at 540 nm associated with the $^3\pi\pi^*$ state of dppn. Instead, the strong feature at 440 nm resembles that observed for $Rh_2$(F-form)$_4$ in $CH_3CN$ ($\lambda_{exc} = 385$ nm) shown in Fig. 11b; the decay of the latter can be fitted to a biexponential function with $\tau_1 = 14$ ps and $\tau_2 = 1$ ns. Since no spectral changes are observed between the two time regimes, the short component is assigned to vibrational cooling and the long component to a triplet excited state. Calculations reveal that in $Rh_2$(F-form)$_4$, the lowest energy triplet state is $^3$MC/$^3$LMCT (LMCT = ligand-to-metal charge transfer) with 95% contribution from the HOMO to the LUMO. The HOMO is composed of 57% F-form and 43% $Rh_2(\delta^*)$ character and the LUMO has 90% contribution from $Rh_2(\sigma^*)$. Therefore the triplet state in $Rh_2$(F-form)$_4$ may be ascribed as a $Rh_2(\delta^*)$/F-form $\rightarrow$ $Rh_2(\sigma^*)$. A comparison of the data presented in Fig. 11a and b suggests that electron density in the $Rh_2(\sigma^*)$ orbital results in the sharp feature at ~440 nm in the two complexes. Similar results are observed for $Rh_2(DTolF)_4$ (Fig. S11 ESI†). Moreover, the broad absorption in the 500–700 nm range in $Rh_2$(F-form)$_4$ may be associated with the oxidized F-form ligand, a feature that is also observed in the spectra of the LLCT state of **5** and **6** (Fig. S9, ESI†).

Similar spectral features and kinetics to those of **7** are observed for **3**, with $\tau_1 = 1$ ps and $\tau_2 = 21$ ps fitted at 435 nm, assigned to vibrational cooling and the DTolF $\rightarrow$ dppn LLCT excited state, respectively (Fig. S9c, ESI†). The formation and decay ($\tau = 490$ ps) of the dppn $^3\pi\pi^*$ state with a maximum at 540 nm is also observed, but the signal of this species is not as pronounced as that observed for **7**. A long-lived component with $\tau = 3.0$ μs associated with an equilibrium between the dppn $^3\pi\pi^*$ and the $^3$MC states is also apparent following 355 nm (fwhm = 8 ns) excitation, as described in more detail in the next section. The lower intensity of the $^3\pi\pi^*$ state observed for **3** as compared to **7** may be due to a difference in the relative energies of the $^3\pi\pi^*$ and the $^3$MC states in the two complexes.

### Excited state manifolds and oxidation potentials

A generalized Jablonski diagram for **1**, **2**, **5** and **6** is depicted in Fig. 12a, where it is assumed that the LLCT state with $\tau \sim 17$–100 ps in these complexes is a singlet, and the 3–8 ps component is assigned to vibrational cooling. Decay of the $^1$LLCT state results in the formation of the $^3$MC state in each complex with lifetimes that range from 40 to 100 ns (Fig. 12a).

In the two dppn-containing complexes, **3** and **7**, the $^3\pi\pi^*$ states are calculated to lie below the $^3$MC state in each complex, but experimental data indicate that this is not the case. The results support a model wherein the $^3\pi\pi^*$ and $^3$MC states are close in energy, and are in fast pre-equilibrium such that the decay from the $^3$MC state to the $^1$GS is the rate limiting step. Similar results were reported previously for Ru(II) complexes where the $^3$MC state lies at an energy close the $^3$MLCT state.[57] Unfortunately, calculation of the pre-equilibrium rate constants is not possible in this case because of spectral overlap of the $^1$LLCT, $^3\pi\pi^*$ and $^3$MC states. The Jablonski diagram for **3** and **7** is depicted in Fig. 12b. The difference in energy of the states between the calculations and the experiments is likely due to the fact that the lowest energy triplet state was calculated vertically from the minimized geometry of the $^1$GS. The calculations, however, do indicate that both the $^3\pi\pi^*$ states of **3** and **7** lie at energies close to the calculated $^3$MC states of **1**, **2**, **5** and **6** which is consistent with the experimental observations. Moreover, the energy of the $^3$MC state of **3** is expected to be nearly the same as those of **1** and **2**, and that for **7** similar to those of **5** and **6**.

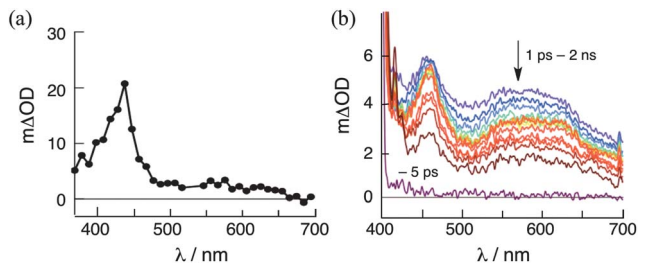


Fig. 11 Transient absorption spectra of (a) **7** collected 1 μs after 355 nm (fwhm = 8 ns) excitation and (b) $Rh_2$(F-form)$_4$ at various time delays after 385 nm excitation (fwhm = 300 fs) in $CH_3CN$.

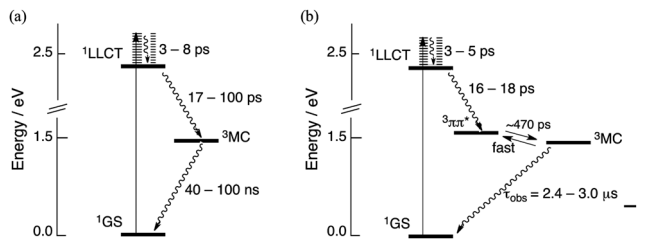


Fig. 12 Generalized Jablonski diagrams for (a) **1**, **2**, **5** and **6**, and (b) **3** and **7**.

Because electron injection to n-type semiconductors in dye-sensitized solar cell assemblies has been shown to be fast and to proceed from the $^1$MLCT state of Ru(II) complexes,[70] it is expected that the $^1$LLCT excited states of **1–3** and **5–7** with lifetimes ranging from 17 to 100 ps should also be able to inject electrons into the conduction bands of semiconductor electrodes. The energy of the $^1$LLCT states, $E_{00}(^1\text{LLCT})$, are calculated to be between 2.3 and 2.4 eV in **1**, **2**, **5** and **6**, at 2.0 eV in **3**, and at 2.1 eV in **7** (Tables S5 and S6, ESI†). These energies are consistent with the observed lowest energy absorption bands in these complexes (Table 1). Given that the first oxidation in **1–3** and **5–7** occurs at ~−0.4 V *vs.* SCE (Table 1), their $^1$LLCT excited state oxidation potentials, $E^*_{ox}(^1\text{LLCT})$, can be calculated to lie between −2.7 and −2.8 V *vs.* SCE for **1**, **2**, **5** and **6**, at −2.5 V *vs.* SCE for **3** and −2.6 V *vs.* SCE for **7**. The lowest energy triplet states of **1**, **2**, **5** and **6**, with calculated $E_{00}(^3\text{MC}) \sim 1.5$ eV, are expected to be less reducing, with $E^*_{ox}(^3\text{MC})$ of approximately −1.8 V *vs.* SCE. These reduction and oxidation processes are illustrated in Fig. 13. Both the singlet and triplet states of the dirhodium(II,II) complexes, however, are significantly better reductants than commonly used Ru(II) complexes. For example, for $[Ru(bpy)_3]^{2+}$, $E^*_{ox}(^1\text{MLCT}) \sim -1.2$ *vs.* SCE and $E^*_{ox}(^3\text{MLCT}) \sim -0.8$ V *vs.* SCE, using $E_{00}(^1\text{MLCT}) \sim 2.5$ eV,[54] $E_{00}(^3\text{MLCT}) \sim 2.1$ eV and $E_{1/2}([\text{Ru}]^{3+/2+} = +1.3$ V *vs.* SCE).[71]

The $^1$LLCT excited states of **1–3** are also good oxidizing agents, with $E^*_{red}(^1\text{LLCT}) \sim +1.3$ V *vs.* SCE, and $E^*_{red}(^1\text{LLCT}) \sim +1.4$ V *vs.* SCE for **5–7**. These values are similar to those of the $^1$MLCT excited state of $[Ru(bpy)_3]^{2+}$, with $E^*_{red}(^1\text{MLCT}) \sim +1.2$ V *vs.* SCE. An additional important point is that hole injection from the MLCT states of Ru(II) complexes requires transfer of the hole from the p-type semiconductor to the oxidized metal, which is not in direct contact with the electrode. In contrast, in the dirhodium(II,II) complexes described herein, the hole in the formamidinate ligand in the $^1$LLCT excited state can be placed on the electrode surface through judicious choice of substituents. In addition, binding of the diimine ligand to an n-type semiconductor is also expected to result in electron injection into its conduction band.

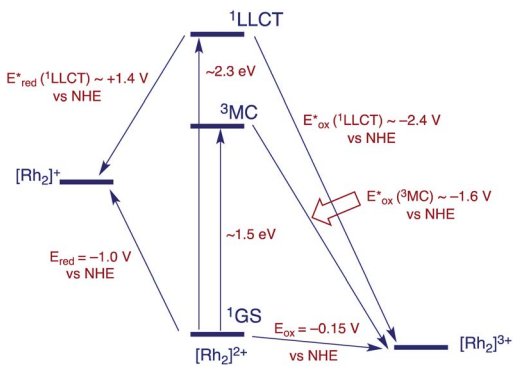


Fig. 13 Latimer diagram showing the ground and excited state oxidation and reduction potentials of **1–3** and **5–7**.

## Conclusions

Two new series of dirhodium(II,II) complexes with electron-rich bridging formamidinate ligands, *cis*-$[Rh_2(\mu\text{-DTolF})_2(L)_2][BF_4]_2$ (**1–3**) and *cis*-$[Rh_2(\mu\text{-F-form})_2(L)_2][BF_4]_2$ (**5–7**), where L = dpq, dppz, dppn, were synthesized and fully characterized by X-ray crystallography and $^1$H NMR spectroscopy. Their electronic and redox properties were investigated in detail as well with the experimental data being augmented by Density Functional Theory results. All of the complexes display one redox event at ~−0.4 V assigned as an oxidation process which is fully supported by chemical oxidation experiments. Both experiment and theory led to the assignment of the low energy electronic absorption bands exhibited by **1–3** and **5–7** to electronic transitions from the HOMO to the LUMO, which corresponds to a ligand-to-ligand charge transfer (LLCT) from the formamidinate to the diimine ligand. Ultrafast transient absorption spectroscopy was used to gain more insight into the excited state processes in these compounds. The LLCT excited states of **1–3** and **5–7** decay with lifetimes that range from 16 to 100 ps, followed by the formation of a longer-lived excited state. For complexes **1**, **2**, **5** and **6**, the latter states exhibit lifetimes ranging from 40 to 100 ns and are assigned as $^3$MC states arising from the $Rh_2(\pi^*) \rightarrow Rh_2(\sigma^*)$ transitions. For **3** and **7**, however, the spectral signature of the dppn-centered $^3\pi\pi^*$ excited state is observed from ~10 ps to ~2 ns; this state decays to form the $^3$MC state of each complex which return to the ground state with lifetimes of 2.4 and 3.0 μs, respectively. The relatively long lifetimes for **3** and **7** are ascribed to a fast pre-equilibrium between the two low-lying $^3\pi\pi^*$ and $^3$MC states. The excited state oxidation potential of the $^1$LLCT state, $E^*_{ox}(^1\text{LLCT})$, for the two series of complexes were calculated to lie between −2.5 and −2.8 V *vs.* SCE and from the $^3$MC state, $E^*_{ox}(^3\text{MC}) \sim -1.8$ V *vs.* SCE. In addition, the excited state reduction potential of the $^1$LLCT excited state, $E^*_{red}(^1\text{LLCT})$, is estimated to be ~+1.3 V *vs.* SCE, such that the complexes are significantly superior oxidizing and reducing agents than commonly used Ru(II) complexes. The excited state redox properties of the two new series of complexes make them excellent candidates for further investigation as the sensitizers in dye-sensitized solar cells due to their potential to inject electrons in the conduction bands and holes in the valence bands of n-type an p-type wide band gap semiconductors, respectively. These investigations are in progress.

## Acknowledgements

K. R. D. and C. T. thank the National Science Foundation for partial support of this work (CHE-1213646), the Ohio Supercomputer Center, and the Center for Chemical and Biochemical Dynamics (CCBD) at OSU. The authors gratefully acknowledge Dr L. M. Pérez for her assistance with the computational studies and the Super Computing Facility and the Laboratory for Molecular Simulation (National Science Foundation CHE-0541587) at Texas A&M University for providing software and computer time. The use of the TAMU/LBMS-Applications Laboratory (Laboratory of Biological Mass Spectroscopy) is also

acknowledged. Use of the Advanced Photon Source was supported by the U. S. Department of Energy, Office of Science, Office of Basic Energy Sciences, under Contract no. DE-AC02-06CH11357.

## Notes and references


1 M. Grätzel, *Philos. Trans. R. Soc. London, Ser. A*, 2007, **365**, 993–1005.

2 J. L. Dempsey, B. S. Brunschwig, J. R. Winkler and H. B. Gray, *Acc. Chem. Res.*, 2009, **42**, 1995–2004.

3 (*a*) T. S. Teets and D. G. Nocera, *Chem. Commun.*, 2011, **47**, 9268–9274; (*b*) A. J. Esswein and D. G. Nocera, *Chem. Rev.*, 2007, **107**, 4022–4047; (*c*) N. S. Lewis and D. G. Nocera, *Proc. Natl. Acad. Sci. U. S. A.*, 2006, **103**, 15729–15735.

4 (*a*) L. Alibabaei, H. Luo, R. L. House, P. G. Hoertz, R. Lopez and T. J. Meyer, *J. Mater. Chem. A*, 2013, **1**, 4133–4145; (*b*) J. J. Concepcion, R. L. House, J. M. Papanikolas and T. J. Meyer, *Proc. Natl. Acad. Sci. U. S. A.*, 2012, **109**, 15560–15564.

5 L. Sun, L. Hammarström, B. Åkermark and S. Styring, *Chem. Soc. Rev.*, 2001, **30**, 36–49.

6 (*a*) W. T. Eckenhoff and R. Eisenberg, *Dalton Trans.*, 2012, **41**, 13004–13021; (*b*) P. Du and R. Eisenberg, *Energy Environ. Sci.*, 2012, **5**, 6012–6021; (*c*) R. Eisenberg, *Science*, 2009, **324**, 44–45.

7 (*a*) G. J. Meyer, *ACS Nano*, 2010, **4**, 4337–4343; (*b*) A. J. Morris, G. J. Meyer and E. Fujita, *Acc. Chem. Res.*, 2009, **42**, 1983–1994.

8 J. Wang, S. M. Arachchige and K. J. Brewer, in *Applications of Supramolecular Chemistry*, ed H. Schneider, CRC Press, Boca Raton, FL, 2012, pp. 255–300.

9 (*a*) B. Kumar, M. Llorente, J. Froehlich, T. Dang, A. Sathrum and C. P. Kubiak, *Annu. Rev. Phys. Chem.*, 2012, **63**, 541–569; (*b*) E. E. Benson, C. P. Kubiak, A. J. Sathrum and J. M. Smieja, *Chem. Soc. Rev.*, 2009, **38**, 89–99.

10 V. Artero, M. Chavarot-Kerlidou and M. Fontecave, *Angew. Chem., Int. Ed.*, 2011, **50**, 7238–7266.

11 S. Losse, J. G. Vos and S. Rau, *Coord. Chem. Rev.*, 2010, **254**, 2492–2504.

12 M. Hartmann, S. Kullmann and H. Keller, *J. Mater. Chem.*, 2010, **20**, 9002–9017.

13 Z. Stasicka, *Adv. Inorg. Chem.*, 2011, **63**, 291–343.

14 (*a*) T. A. White, J. D. Knoll, S. M. Arachchige and K. J. Brewer, *Materials*, 2011, **5**, 27–46; (*b*) T. A. White, S. L. H. Higgins, S. M. Arachchige and K. J. Brewer, *Angew. Chem., Int. Ed.*, 2011, **50**, 12209–12213; (*c*) T. A. White, B. N. Whitaker and K. J. Brewer, *J. Am. Chem. Soc.*, 2011, **133**, 15332–15334.

15 S. Fukuzumi, Y. Yamada, T. Suenobu, K. Ohkubo and H. Kotani, *Energy Environ. Sci.*, 2011, **4**, 2754–2766.

16 (*a*) P. Du, K. Knowles, J. Schneider and R. Eisenberg, *J. Am. Chem. Soc.*, 2008, **130**, 12576–12577; (*b*) P. Du, J. Schneider, G. Luo, W. W. Brennessel and R. Eisenberg, *Inorg. Chem.*, 2009, **48**, 4952–4962.

17 (*a*) J. D. Knoll, S. M. Arachchige and K. J. Brewer, *ChemSusChem*, 2011, **4**, 252–261; (*b*) G. F. Manbeck and K. J. Brewer, *Coord. Chem. Rev.*, 2013, **257**, 1660–1675.

18 (*a*) A. Fihri, V. Artero, A. Pereira and M. Fontecave, *Dalton Trans.*, 2008, 5567–5569; (*b*) A. Fihri, V. Artero, M. Razavet, C. Baffert, W. Leibl and M. Fontecave, *Angew. Chem., Int. Ed.*, 2008, **47**, 564–567.

19 S. Jasimuddin, T. Yamada, K. Fukuju, J. Otsuki and K. Sakai, *Chem. Commun.*, 2010, **46**, 8466–8468.

20 B. Probst, A. Rodenberg, M. Guttentag, P. Hamm and R. Alberto, *Inorg. Chem.*, 2010, **49**, 6453–6460.

21 J. Xie, C. Li, Q. Zhou, W. Wang, Y. Hou, B. Zhang and X. Wang, *Inorg. Chem.*, 2012, **51**, 6376–6384.

22 (*a*) A. F. Heyduk and D. G. Nocera, *Science*, 2001, **293**, 1639–1641; (*b*) A. J. Esswein, A. S. Veige and D. G. Nocera, *J. Am. Chem. Soc.*, 2005, **127**, 16641–16651; (*c*) C. H. Lee, T. R. Cook and D. G. Nocera, *Inorg. Chem.*, 2011, **50**, 714–716; (*d*) N. Elgrishi, T. S. Teets, M. B. Chambers and D. G. Nocera, *Chem. Commun.*, 2012, **48**, 9474–9476.

23 P. G. Bomben, K. C. D. Robson, B. D. Koivisto and C. P. Berlinguette, *Coord. Chem. Rev.*, 2012, **256**, 1438–1450.

24 (*a*) J.-F. Yin, M. Velayduham, D. Bhattacharya, H.-C. Lin and K.-L. Lu, *Coord. Chem. Rev.*, 2012, **256**, 3008–3035; (*b*) G. F. Moore, S. J. Konezny, H. Song, R. L. Milot, J. D. Blakemore, M. L. Lee, V. S. Batista, C. A. Schmuttenmaer, R. H. Crabtree and G. W. Brudvig, *J. Phys. Chem. C*, 2012, **116**, 4892–4902.

25 M. Buchalska, J. Kuncewicz, E. Świętek, P. Labuz, T. Baran, G. Stochel and W. Macyk, *Coord. Chem. Rev.*, 2013, **257**, 767–775.

26 F. Odobel, L. L. Pleux, Y. Pellegrin and E. Blart, *Acc. Chem. Res.*, 2010, **43**, 1063–1071.

27 A. M. McDaniel, H. W. Tseng, N. H. Damrauer and M. P. Shores, *Inorg. Chem.*, 2010, **49**, 7981–7991.

28 P. Qin, H. Zhu, T. Edvinsson, G. Boschloo, A. Hagfeldt and L. Sun, *J. Am. Chem. Soc.*, 2008, **130**, 8570–8572.

29 J. He, H. Lindström, A. Hagfeldt and S. Lidnquist, *Sol. Energy Mater. Sol. Cells*, 2000, **62**, 265–273.

30 A. Nattestad, A. J. Mozer, M. K. R. Fischer, Y.-B. Cheng, A. Mishra, P. Bäuerle and U. Bach, *Nat. Mater.*, 2009, **9**, 31–35.

31 N. Tétreault, L.-P. Heiniger, M. Stefik, P. P. Labouchère, É. Arsenault, N. K. Nazeeruddin, G. A. Ozin and M. Grätzel, *ECS Trans.*, 2011, 303–314.

32 J. Gong, J. Liang and K. Sumathy, *Renewable Sustainable Energy Rev.*, 2012, **16**, 5848–5860.

33 M. Grätzel, *Nature*, 2001, **414**, 338–344.

34 C. G. Van de Walle and J. Neugebauer, *Nature*, 2003, **423**, 626–628.

35 D. A. Lutterman, N. N. Degtyareva, D. H. Johnston, J. C. Gallucci, J. L. Eglin and C. Turro, *Inorg. Chem.*, 2005, **44**, 5388–5396.

36 (*a*) K. V. Catalan, J. S. Hess, M. M. Maloney, D. J. Mindiola, D. L. Ward and K. R. Dunbar, *Inorg. Chem.*, 1999, **38**, 3904–3913; (*b*) H. T. Chifotides, K. V. Catalan and K. R. Dunbar, *Inorg. Chem.*, 2003, **42**, 8739–8747.

37 A. M. Angeles-Boza, P. M. Bradley, P. K. L. Fu, S. E. Wicke, J. Bacsa, K. R. Dunbar and C. Turro, *Inorg. Chem.*, 2004, **43**, 8510–8519.


 

38 K. R. Mann, R. A. Bell and H. B. Gray, *Inorg. Chem.*, 1979, **18**, 2671–2673.

39 Y. Sun, L. E. Joyce, N. M. Dickson and C. Turro, *Chem. Commun.*, 2010, **46**, 2426–2428.

40 (*a*) A. M. Angeles-Boza, P. M. Bradley, P. K. L. Fu, M. Shatruk, M. G. Hilfiger, K. R. Dunbar and C. Turro, *Inorg. Chem.*, 2005, **44**, 7262–7264; (*b*) J. D. Aguirre, A. M. Angleles-Boza, A. Chouai, J.-P. Pellois, C. Turro and K. R. Dunbar, *J. Am. Chem. Soc.*, 2009, **131**, 11353–11360; (*c*) L. E. Joyce, J. D. Aguirre, A. M. Angeles-Boza, A. Chouai, P. K.-L. Fu, K. R. Dunbar and C. Turro, *Inorg. Chem.*, 2010, **49**, 5371–5376.

41 (*a*) R. E. Holmlin, J. A. Yao and J. K. Barton, *Inorg. Chem.*, 1999, **38**, 174–189; (*b*) R. E. Holmlin, E. D. A. Stemp and J. K. Barton, *J. Am. Chem. Soc.*, 1996, **118**, 5236–5244; (*c*) R. B. Nair, E. S. Teng, S. L. Kirkland and C. J. Murphy, *Inorg. Chem.*, 1998, **37**, 139–141.

42 Y. Sun, L. E. Joyce, N. M. Dickson and C. Turro, *Chem. Commun.*, 2010, **46**, 6759–6761.

43 Y. Liu, R. Hammitt, D. A. Lutterman, L. E. Joyce, R. P. Thummel and C. Turro, *Inorg. Chem.*, 2009, **48**, 375–385.

44 Y. Sun, D. A. Lutterman and C. Turro, *Inorg. Chem.*, 2008, **47**, 6427–6434.

45 T. Joshi, G. J. Barbante, P. S. Francis, C. F. Hogan, A. M. Bond and L. Spiccia, *Inorg. Chem.*, 2011, **50**, 12172–12183.

46 X. W. Liu, J. Li, H. Deng, K. C. Zheng, Z. W. Mao and L. N. Ji, *Inorg. Chim. Acta*, 2005, **358**, 3311–3319.

47 N. G. Connelly and W. E. Geiger, *Chem. Rev.*, 1996, **96**, 877–910.

48 M. Inoue and M. B. Inoue, *J. Chem. Soc., Faraday Trans. 2*, 1985, **81**, 539–547.

49 T. Ren, C. Lin, E. J. Valente and J. D. Zubkowski, *Inorg. Chim. Acta*, 2000, **297**, 283–290.

50 S. Delaney, M. Pascaly, P. K. Bhattacharya, K. Han and J. K. Barton, *Inorg. Chem.*, 2002, **41**, 1966–1974.

51 (*a*) A. E. Bragg, G. U. Kanu and B. J. Schwartz, *J. Phys. Chem. Lett.*, 2011, **2**, 2797–2804; (*b*) H. Prakash and P. Natarajan, *J. Photochem. Photobiol., A*, 2004, **168**, 81–90; (*c*) C. Selvaraju and P. Ramamurthy, *Chem.–Eur. J.*, 2004, **10**, 2253–2262; (*d*) J. H. Baxendale, C. Bell and P. Wardman, *Chem. Phys. Lett.*, 1971, **12**, 347–348.

52 M. Chergui, *Dalton Trans.*, 2012, **41**, 13022–13029.

53 A. Cannizzo, F. van Mourik, W. Gawelda, G. Zgrablic, C. Bressler and M. Chergui, *Angew. Chem., Int. Ed.*, 2006, **45**, 3174–3176.

54 A. C. Bhasikuttan, M. Suzuki, S. Nakashima and T. Okada, *J. Am. Chem. Soc.*, 2002, **124**, 8398–8405.

55 (*a*) Y. Sun, Y. Liu and C. Turro, *J. Am. Chem. Soc.*, 2010, **132**, 5594–5595; (*b*) B. Peña, N. A. Leed, K. R. Dunbar and C. Turro, *J. Phys. Chem. C*, 2012, **116**, 22186–22195; (*c*) Y. Liu, D. B. Turner, T. N. Singh, A. M. Angeles-Boza, A. Chouai, K. R. Dunbar and C. Turro, *J. Am. Chem. Soc.*, 2009, **131**, 26–27.

56 (*a*) A. A. Rachford and J. J. Rack, *J. Am. Chem. Soc.*, 2006, **128**, 14318–14324; (*b*) D. A. Lutterman, A. A. Rachford, J. J. Rack and C. Turro, *J. Phys. Chem. Lett.*, 2010, **1**, 3371–3375; (*c*) A. W. King, Y. Jin, J. T. Engle, C. J. Ziegler and J. J. Rack, *Inorg. Chem.*, 2013, **52**, 2086–2093.

57 J. T. Hewitt, P. J. Vallet and N. H. Damrauer, *J. Phys. Chem. A*, 2012, **116**, 11536–11547.

58 A. Cannizzo, A. M. Blanco-Rodríguez, A. E. Nahhas, J. Šebera, S. Zalis, A. Vlček and M. Chergui, *J. Am. Chem. Soc.*, 2008, **130**, 8967–8974.

59 (*a*) E. A. Juban, A. L. Smeigh, J. E. Monat and J. K. McCusker, *Coord. Chem. Rev.*, 2006, **250**, 1783–1791; (*b*) J. N. Schrauben, K. L. Dillman, W. F. Beck and J. K. McCusker, *Chem. Sci.*, 2010, **1**, 405–410.

60 C. Bressler, C. Milne, V.-T. Pham, A. EINahhas, M. van der Veen, W. Gawelda, S. Johnson, P. Beaud, D. Grolimund, M. Kaiser, C. N. Borca, G. Ingold, R. Abela and M. Chergui, *Science*, 2009, **323**, 489–492.

61 A. L. Smeigh, M. Creelman, R. A. Mathies and J. J. McCusker, *J. Am. Chem. Soc.*, 2008, **130**, 14105–14107.

62 M. H. Chisholm, T. L. Gustafson and C. Turro, *Acc. Chem. Res.*, 2013, **46**, 529–538.

63 A. E. Stiegman, S. F. Rice, H. B. Gray and V. M. Miskowski, *Inorg. Chem.*, 1987, **26**, 1112–1116.

64 R. M. van der Veen, A. Cannizzo, F. van Mourik, A. Vlček, Jr and M. Chergui, *J. Am. Chem. Soc.*, 2011, **133**, 305–315.

65 V. M. Miskowski, S. F. Rice, S. J. Milder and H. B. Gray, *J. Phys. Chem.*, 1993, **97**, 4277–4283.

66 G. T. Ruiz, M. P. Juliarena, R. O. Lezna, M. R. Feliz and G. Ferraudi, *J. Photochem. Photobiol., A*, 2006, **179**, 289–297.

67 Y. Sun, L. E. Joyce, N. M. Dickson and C. Turro, *Chem. Commun.*, 2010, **46**, 2426–2428.

68 L. E. Joyce, J. D. Aguirre, A. M. Angeles-Boza, A. Chouai, P. K.-L. Fu, K. R. Dunbar and C. Turro, *Inorg. Chem.*, 2010, **49**, 5371–5376.

69 (*a*) Y. Liu, R. Hammitt, D. A. Lutterman, L. E. Joyce, R. P. Thummel and C. Turro, *Inorg. Chem.*, 2009, **48**, 375–385; (*b*) R. Zhao, R. Hammitt, R. P. Thummel, Y. Liu, C. Turro and R. M. Snapka, *Dalton Trans.*, 2009, 10926–10931.

70 N. A. Anderson and T. Lian, *Coord. Chem. Rev.*, 2004, **248**, 1231–1246.

71 A. Juris, V. Balzani, F. Barigelletti, S. Campagna, P. Belser and A. von Zelewsky, *Coord. Chem. Rev.*, 1988, **84**, 85–277.